

Low Cycle Fatigue Behavior of a Directionally Solidified Nickel-Based Superalloy: Mechanistic and Microstructural Aspect



R.K. RAI, J.K. SAHU, N. PAULOSE, and C. FERNANDO

In the present research, efforts were made to understand the mechanistic and microstructural aspects of the low cycle fatigue failure of a directionally solidified (DS) nickel-based superalloy under relevant operating conditions. The differences between the dislocation structures observed during different temperatures and strain amplitudes are clearly shown in the transmission electron (TEM) micrographs and are giving rise to the divergence in associated LCF responses. The deformation mechanism changes as a function of temperature. While shearing of γ' -precipitates by stacking faults is the dominant deformation mechanism at the lowest temperature (750 °C), γ' -coarsening and dislocation networks are prevalent at the highest temperatures (930 °C). Mixed deformation behavior is observed at the intermediate temperature (850 °C). Constituent's phases of the alloy also play crucial roles during deformation.

<https://doi.org/10.1007/s11661-020-05720-5>

© The Minerals, Metals & Materials Society and ASM International 2020

I. INTRODUCTION

DIRECTIONALLY solidified nickel-based superalloys are used to construct the hot section components like turbine blades and vanes of aero-engines.^[1–5] During the service, the blade materials experience fluctuating thermal stresses, which accentuates the need to possess exceptionally good high-temperature low cycle fatigue (LCF) resistance.^[6–9] The LCF deformation behavior of the blade material, therefore, has attracted interest in the past decades.^[6,8–11] To prevent the premature replacement of such an expensive component and to avoid economic/human casualties, fatigue life prediction is of paramount importance. It is worth mentioning that the success of a life prediction scheme requires a proper consciousness of LCF damage micromechanisms at various temperatures.^[12–15] Microstructural evolution during service exposure has a sizable effect on the LCF damage micromechanisms and fatigue life.^[14–21] Therefore, it is extremely important to understand the microstructural alterations and damage mechanisms during service exposure. Despite all the efforts, a universally acceptable fatigue life prediction scheme is still scarce.^[20–22] Some of the life

prediction schemes work effectively for certain alloy systems, but not as well for others. The different forms of damage that originated in various alloy systems are the main culprit for it.^[22–24]

The chemistry of the directionally solidified (DS) nickel-based superalloy used in the present study evolved from that of MAR-M 247 alloy, which is designed for the turbine blade application.^[1] However, to enhance the creep and LCF resistance required for the blade application, the chemical composition and heat treatment of the alloy was altered.^[1] The tensile and creep deformation behaviors of the DS alloy were discussed by the authors recently.^[25,26] Those studies^[25,26] revealed that both tensile and creep deformation behaviors of the alloy are highly sensitive to the testing temperatures and microstructural stabilities. Non-uniform planar slip, involving precipitates shearing by $a/2 \langle 110 \rangle$ and $a/3 \langle 112 \rangle$ dislocation partials, was found to be the dominant deformation mechanism at the lower temperatures whereas homogeneous slip resulting from dislocation bypass mechanisms is dominant at the higher temperatures ($T > 850$ °C). In addition to it, precipitate coarsening and oxidation occurring at a higher temperature also play a crucial role during deformation.^[25,26] Given the dominating effect of temperature on the deformation behavior, the LCF damage mechanisms of the DS alloy were assessed under pertaining conditions.

An in-depth understanding of LCF deformation, micromechanisms of the alloy will bestow the opportunity to assess the weak links or damage initiation sites in the microstructure, which can be essential inputs for the designers. Such a study could not be found for the present alloy. It is worth noticing that the web of DS

R.K. RAI is with the AcSIR, CSIR-National Metallurgical Laboratory, Jamshedpur 831007, India. Contact e-mail: rajeshrai.bits@yahoo.in J.K. SAHU is with the CSIR-National Metallurgical Laboratory, Jamshedpur 831007, India. N. PAULOSE and C. FERNANDO are with the Gas Turbine Research Establishment, Bangalore 560093, India.

Manuscript submitted on August 1, 2019.

Article published online March 14, 2020

turbine blades is exposed to the intermediate temperatures, mostly at 750 °C to 850 °C, whereas higher temperature, 930 °C, is encountered at the blade tip; therefore, the evaluation of mechanical properties is very critical at these temperatures.

In the present study, therefore, the LCF deformation behavior of a DS nickel-based superalloy was investigated in the temperature range of 750 °C to 930 °C at different values of $\Delta\epsilon/2$. The concomitant microstructures of the fatigue-fractured specimens were comprehensively discussed in relation to the macroscopic fatigue response. A tenable explanation based on the microstructural evolution has been proposed for the change in fatigue deformation mechanism and fatigue life during service exposure.

II. EXPERIMENTAL

A. Material and Heat Treatment

The DS alloy in the form of rods of dimensions (diameter = 15.00 mm and length = 135.00 mm) was received in the heat-treated conditions. Chemical composition (wt pct) of the investigated alloy is as follows: Cr-8Co-9.3Al-5.58Mo-0.05Ti-0.74W-9.49-Ta-3.2C-0.07Hf-1.41B-0.018Zr-0.009 and balance Ni. The heat treatments given to the alloy are as follows: solution treatment; 1230 °C to 1240 °C/8 hours/gas fan quenching (GFQ) + aging treatments; 1080 °C/4 hours/GFQ + 870 °C/20 hours/GFQ.^[27]

B. Mechanical Testing

All the LCF tests were conducted at $R = 0$ under axial strain control mode in air, by using a triangular strain cycle with total strain amplitude ($\Delta\epsilon/2$) values ranging from 0.4 to 0.8 pct and at 750 °C, 850 °C, and 930 °C. Tensile tests were also conducted at the same temperatures. The strain rate employed during the LCF and tensile tests was $1 \times 10^{-3} \text{ s}^{-1}$. The LCF and tensile tests were conducted as per the ASTM standards E-606-12 and E-08, respectively, on smooth polished cylindrical specimens in an INSTRON 8862 servo-electric machine of load capacity 100 KN. Figure 1 illustrates the dimensional drawing of both LCF and tensile test specimens used in the present study. The heating of the test specimens was done by using the resistance furnace attached to the INSTRON machine. PID controller was used to controlling the temperature during both fatigue and tensile tests. The temperature during the tests was monitored using Pt-13 pct Rh thermocouples tied to the gauge length portion. Strain measurements were made using a high-temperature extensometer (Instron: M20-52632-1) having a gauge length of 12.5 mm and a range of travel of ± 20 pct.

C. Frequency Calculation for LCF Tests

Figure 2 shows the schematic of the triangular wave cycle used for LCF testing. The frequency for the LCF tests was calculated as follows:

$$f = \frac{1}{2} \times \frac{\epsilon_r}{\epsilon_{\max}}$$

where f = frequency, ϵ_{\max} = maximum strain and ϵ_r = strain rate.

D. SEM and TEM Characterization

The microstructure of the LCF-tested specimens was observed using a FEG equipped scanning electron microscope (SEM, FEI NOVA Nano SEM 430). For the fractographic examinations, fracture surface perpendicular to the [001] direction of the fatigue tested specimens was sliced and for the SEM micrographs, specimens were sectioned near to the fracture surface and parallel to [001] direction. Samples for the SEM characterization were prepared by employing standard metallographic techniques consisting of paper polishing using 500 to 2500 Si grit papers, which is followed by colloidal silica cloth polishing. Samples for the SEM studies were etched using Aqua regia (10 mL HNO₃ and 30 mL HCl). The substructural examinations were carried out using a FEG transmission electron microscope (JEOL 2200 FS) operating at 200 kV. Samples for TEM examinations were prepared by slicing disks from the LCF-tested specimens perpendicular to the loading axis ([001] direction) followed by electrolytic polishing in a twin-jet electro-polisher (Fischione Instruments) using an electrolyte of 10 pct HClO₄ dissolved in 90 pct CH₃OH at a voltage of 25 V and temperature of -35 °C.

III. RESULTS

A. Microstructure

Figure 3 depicts the SEM micrograph of as-received alloy. The microstructure of DS alloy mainly consists of uniformly distributed cuboidal γ' -precipitates, non-uniformly distributed irregular shaped Hf/Ta rich MC carbides, fine Cr-rich, M₂₃C₆ carbides at the grain boundaries, and γ - γ' eutectic islands.

B. Cyclic Life and Cyclic Hardening/Softening Behavior at Different Temperatures

A comparison of fatigue lives (N_f) of the investigated superalloy at different values of strain amplitude ($\Delta\epsilon/2$) is shown in Figure 4. A considerable drop in N_f is observed (Figure 4) with an increase in testing temperature for all the investigated values of $\Delta\epsilon/2$.

The maximum values of fatigue lives are observed at 750 °C for all the investigated values of $\Delta\epsilon/2$. A similar type of variation of fatigue life in the temperature range, from 760 °C to 871 °C, was also found in the study of LCF behavior of DS nickel-based superalloy René80.^[28]

Figures 5(a) through (c) shows the cyclic stress response of the alloy at 750 °C, 850 °C, and 930 °C for the values of $\Delta\epsilon/2$ ranging from 0.4 to 0.8 pct. It can be observed (Figures 5(a) through (c)) that the

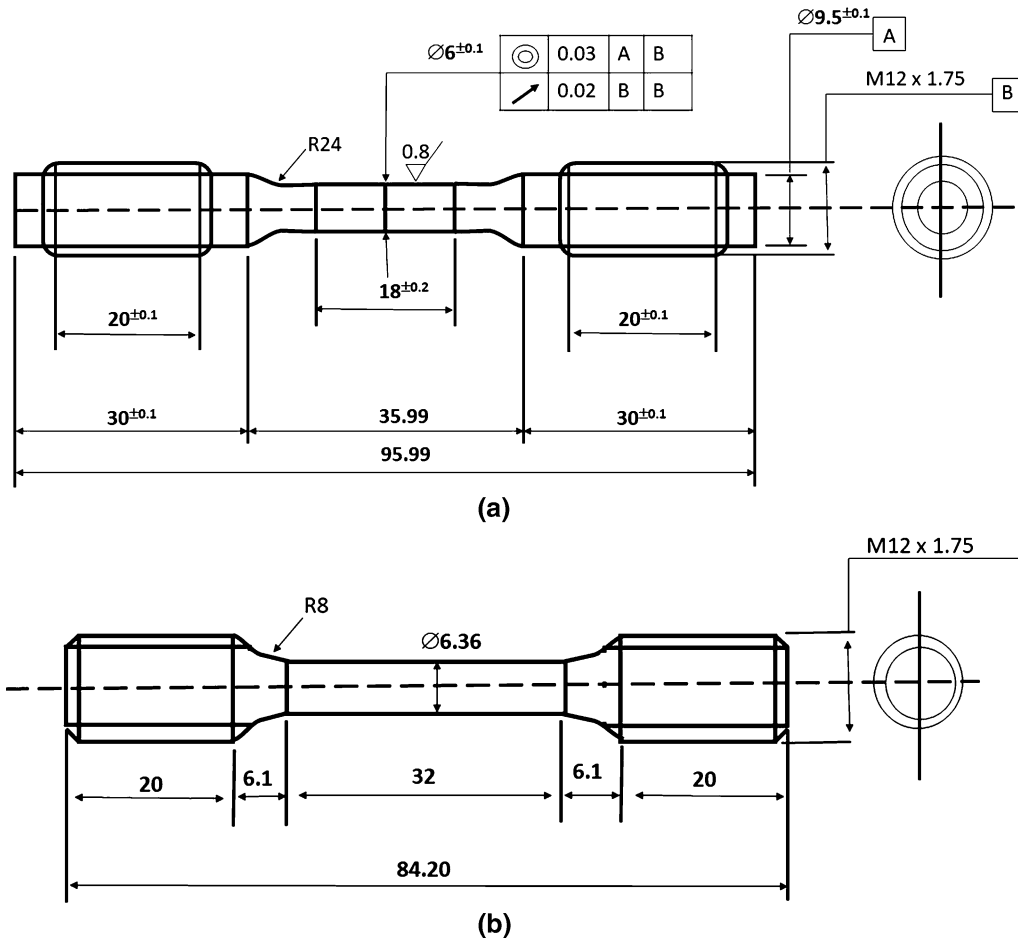


Fig. 1—Dimensional drawing of (a) LCF and (b) tensile test specimens.

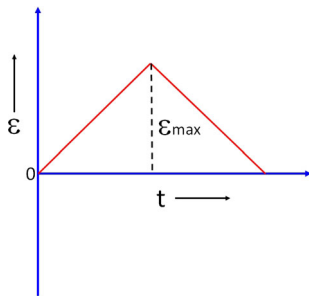


Fig. 2—Schematic showing the triangular wave cycle used for the LCF testing.

deformation behavior of the alloy varied with temperature (T). At $750\text{ }^{\circ}\text{C}$, the alloy exhibits cyclic hardening for the first 2 to 3 cycles, followed by mild softening for all the investigated values of $\Delta\epsilon/2$. In contrast, the alloy displays continuous cyclic softening throughout the fatigue life at $850\text{ }^{\circ}\text{C}$ and $930\text{ }^{\circ}\text{C}$. The extent of cyclic softening is more pronounced at $930\text{ }^{\circ}\text{C}$. Figure 6 depicts the comparison of saturated stress amplitudes ($\Delta\sigma_s/2$) recorded at mid-life for all the investigated values of $\Delta\epsilon/2$. The value of $\Delta\sigma_s/2$ is highest at $750\text{ }^{\circ}\text{C}$ for imposed $\Delta\epsilon/2$ (Figure 6).

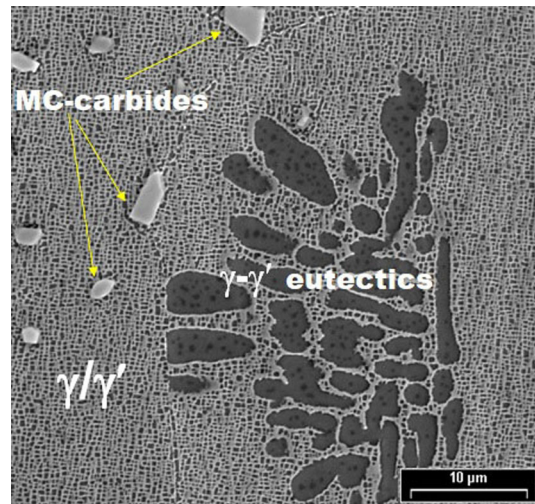


Fig. 3—SEM micrographs of as-received DS alloy.

C. The Cyclic Stress–Strain Curve at Different Temperatures

Cyclic stress–strain (CSS) curves of the investigated superalloy were extracted by plotting the $\Delta\sigma/2$ values obtained at $N_f/2$ against the imposed $\Delta\epsilon/2$. The CSS

curves at the temperatures of 750 °C, 850 °C, and 930 °C were compared with the corresponding monotonic stress–strain, S – e , curves obtained at these temperatures (Figures 7(a) through (c)). It can be observed from Figures 7(a) through (c) that the CSS curves lie below the S – e curves of the investigated temperatures. It has been seen^[29,30] that, when the CSS curve lies below the S – e curve, the alloy exhibits cyclic softening, whereas cyclic hardening behavior is observed under reverse

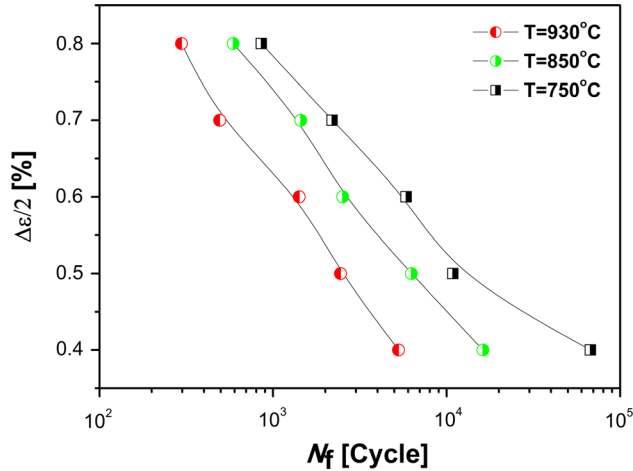
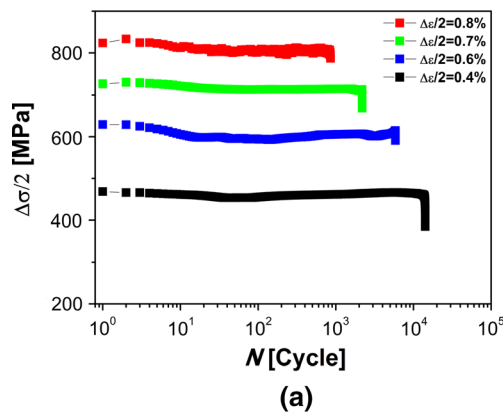
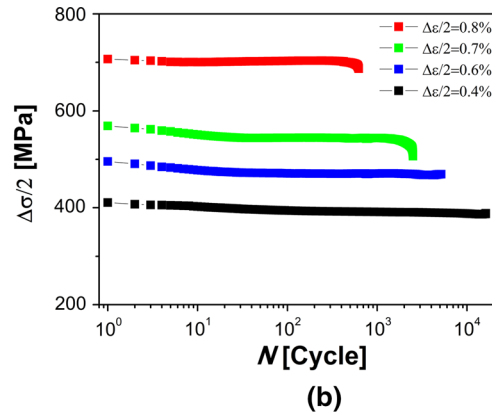


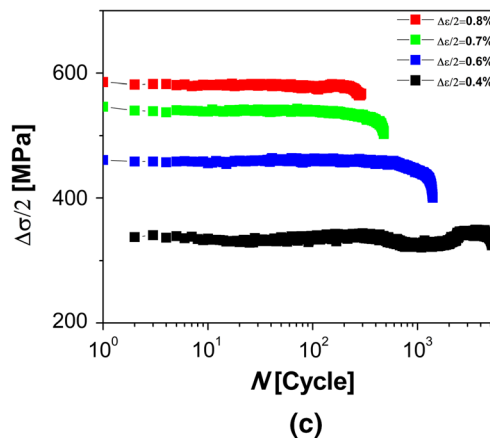
Fig. 4—Fatigue lives at 750 °C, 850 °C, and 930 °C corresponding to $\Delta\epsilon/2$ values of 0.4 to 0.8 pct.



(a)



(b)



(c)

Fig. 5—Cyclic stress response curves at (a) 750 °C, (b) 850 °C, and (c) 950 °C.

condition. The CSS curves (Figures 7(a) through (c)) indicates an obvious cyclic softening at 750 °C, 850 °C, and 930 °C.

The CSS and monotonic behavior were analyzed using the following power-law relationships, respectively^[17]:

$$\frac{\Delta\sigma}{2} = K' \left(\frac{\Delta\epsilon_p}{2} \right)^{n'} \quad [1]$$

$$\sigma = k\epsilon^n \quad [2]$$

where n' and n are cyclic and monotonic strain hardening exponents and K' and k are cyclic and monotonic strength coefficients, σ is the true stress, and $\Delta\epsilon_p/2$ and $\Delta\sigma/2$ are the plastic strain and stress amplitudes at mid-life. The values of all coefficients and exponents determined from Eqs. [1] and [2] are given in Table I. The value of n' (Table I) is highest at 750 °C, which implies that the cyclic hardening is highest at this temperature. These trends have well supported the facts observed from the cyclic stress response curves (Figure 5) and $\Delta\sigma_s/2$ vs $\Delta\epsilon/2$ curves (Figure 6).

D. Mean Stress Effects

Figures 8(a) through (c) shows the variation of mean-stress (σ_{mean}) as a function of fatigue cycles at

the investigated T and $\Delta\epsilon/2$. While significant σ_{mean} has been developed during LCF tests conducted at 750 °C for all $\Delta\epsilon/2$, however, in contrast, negligible σ_{mean} is observed at 930 °C, except at the lower values of $\Delta\epsilon/2$. At the 850 °C, a mixed behavior is observed, where sustained σ_{mean} is almost relaxed at the higher values of $\Delta\epsilon/2$. It is noteworthy that the fatigue failure of a component strongly correlates with the applied $\Delta\epsilon/2$, T , and the σ_{mean} .^[29,30] The σ_{mean} can be a serious concern during lower amplitude LCF tests conducted

at $R = 0$.^[29–31] In their previous research,^[17] the authors have well described the deleterious effect of σ_{mean} on the LCF behavior of the investigated superalloy. During their studies,^[17] the authors have concluded that the presence of sustained σ_{mean} has a profound effect on LCF life, particularly at higher temperatures. The highest fatigue life observed at 750 °C is attributed to the minimal effect of σ_{mean} at the lower temperatures.^[30,32]

E. Smith–Watson–Topper (SWT) Relationship

Fatigue performance (Figure 9) of the alloy was described by employing Smith–Watson–Topper (SWT) relationship^[17,31] represented by Eq. [3]. The SWT parameter grants the approximate value of the energy dissipated during fatigue cycles and describes very well the fatigue life in the presence of mean stress, particularly at the lower values of cyclic plastic strains. In their previous studies, authors have shown that the SWT

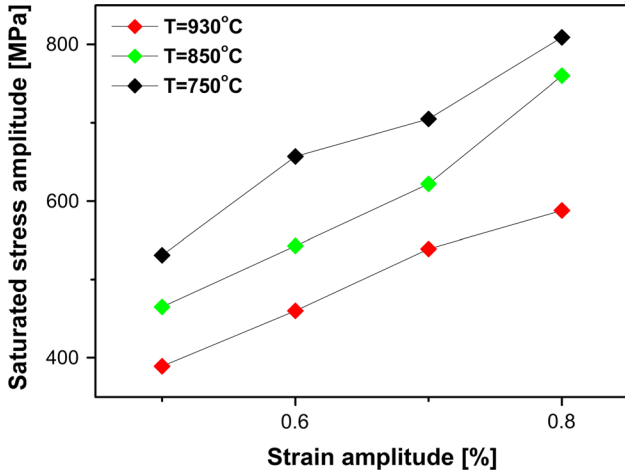


Fig. 6—Comparison of saturated stress amplitudes ($\Delta\sigma_s/2$) recorded at mid-life for the values of $\Delta\epsilon/2$ ranging from 0.4 to 0.8 pct at 750 °C, 850 °C, and 930 °C.

Table I. Values of n' and Λ' at the Investigated Temperatures

Temperatures (°C)	750	850	930
n'	0.6	0.33	0.29
Λ'	1030	2141	1279
n	0.034	0.03	0.12
K	1236	1000	803.3

The value of n' is higher at 750 °C.

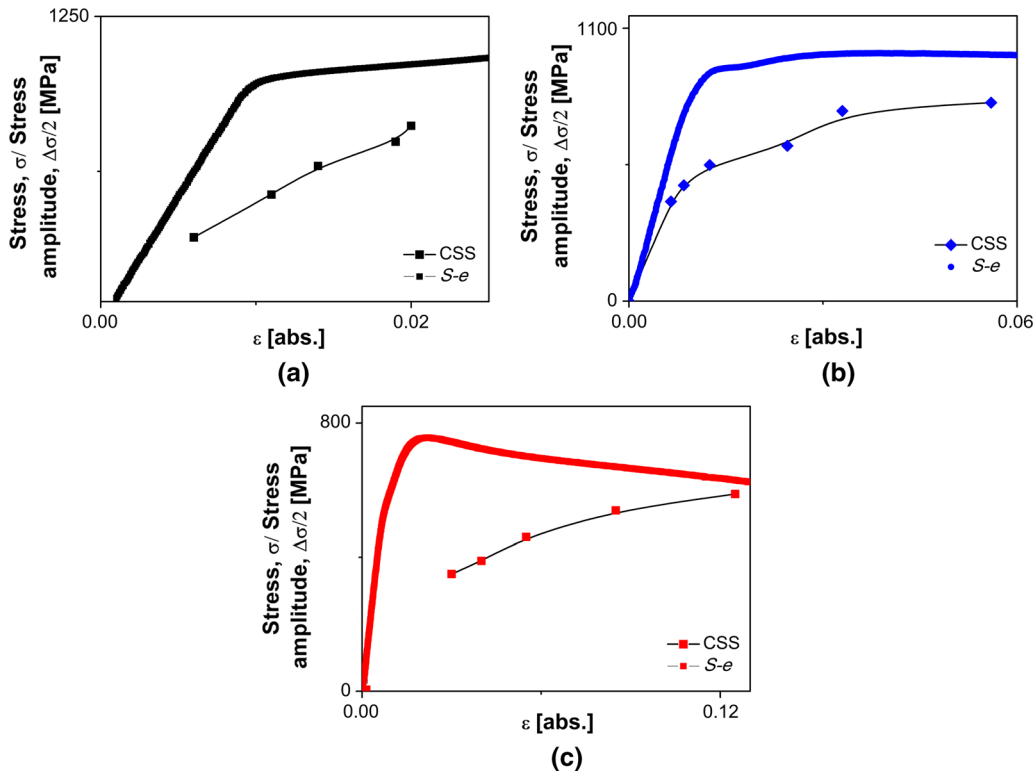


Fig. 7—CSS and monotonic curves: (a) 750 °C, (b) 850 °C, and (c) 930 °C.

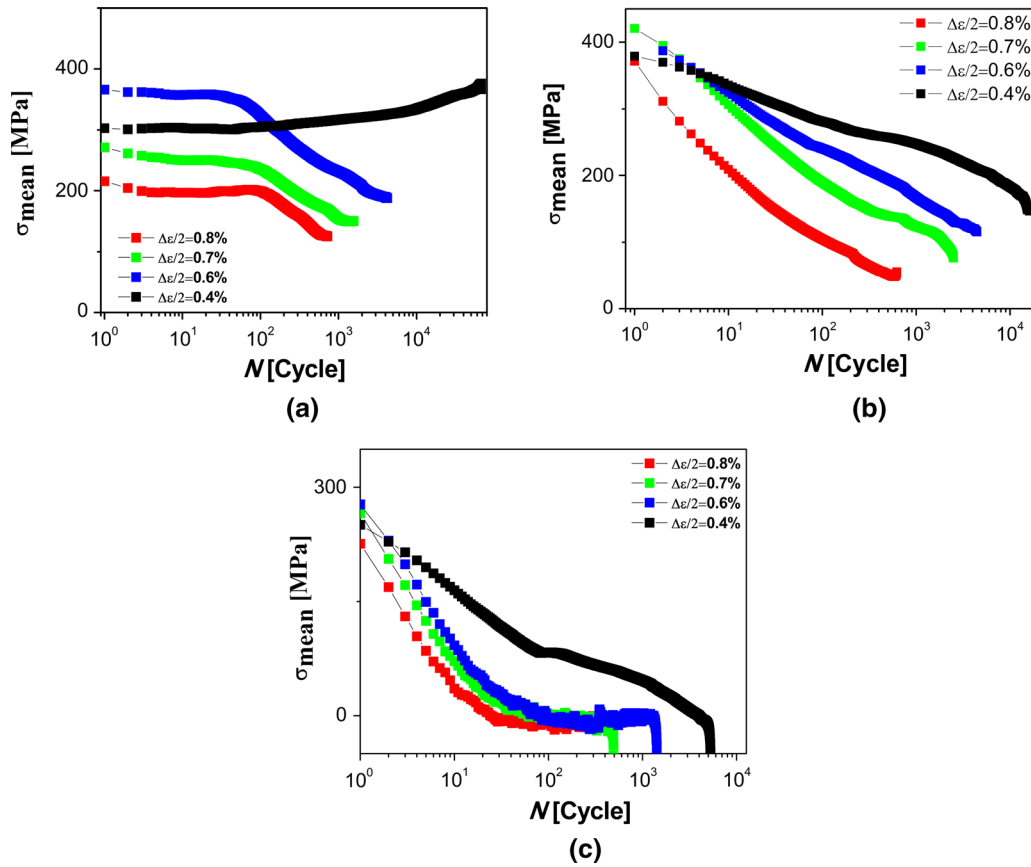


Fig. 8—Mean-stress curves: (a) 750 °C, (b) 850 °C, and (c) 930 °C.

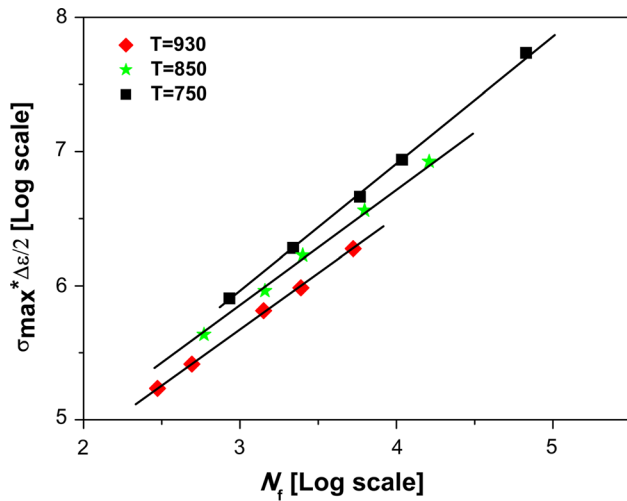


Fig. 9—SWT plots at 750 °C, 850 °C, and 930 °C.

parameter suitably rationalized the fatigue response of the investigated superalloy.^[17,33] The current results are well aligned with the previous work.^[17,33] It is worth mentioning that the slope of the SWT plot is steeper at a lower temperature ($T = 750$ °C) as compared to the high temperatures ($T = 850$ °C and 930 °C).

$$\left(\sigma_{\max} \cdot \frac{\Delta \varepsilon}{2} \right) = \frac{(\sigma'_f)^2}{E} (2N_f)^{2b} + \sigma'_f \varepsilon'_f (2N_f)^{b+c} \quad [3]$$

where σ_{\max} = maximum stress at mid-life of each test; $\Delta \varepsilon / 2$ = total strain amplitude; σ'_f = fatigue strength coefficient; ε'_f = fatigue ductility coefficient; b = fatigue strength exponent; and c = fatigue ductility exponent.

F. SEM and Fractographic Examinations of LCF-Tested Specimens

Figure 10 shows typical fracture surface and SEM micrographs (sectioned near to the fracture surface and parallel to [001] direction) of the alloy after fatigue test performed at 750 °C and $\Delta \varepsilon / 2$ of 0.5 pct. It can be observed from Figures 10(a) and (b) that the cracks are initiated from the specimen surface (marked by a dotted line in Figure 10(a)). It is evident (Figures 10(a) and (b)) that the crack initiation area is very smooth, which is the characteristic of crystallographic or quasi-cleavage fracture.^[11–14] Such cracking occurred along the cellular γ' -precipitates (marked circles in Figure 10(c)) located at the specimen surface. It is noteworthy to mention that such layers of cellular γ' -precipitates were only observed during fatigue deformation of the alloy at 750 °C. These cellular γ' -precipitates have equiaxed morphology and are smaller in size as compared to the big ellipsoidal γ - γ' eutectics present in the as-received alloy. Figure 10(d)

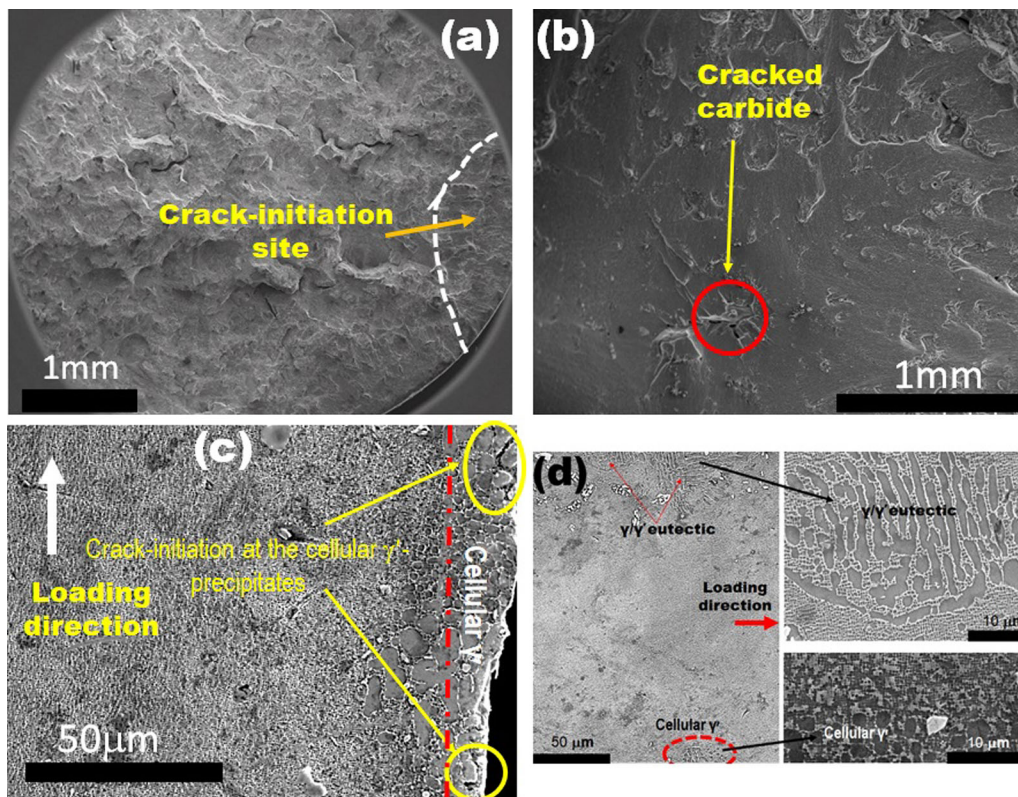


Fig. 10—(a, b) Fracture surfaces and (c) SEM micrograph of the specimen fatigue ruptured at 750 °C and $\Delta\epsilon/2$ of 0.5 pct. The area marked by the white circle in (b) and the yellow circle in (c) showing crack initiations at the cellular γ' -precipitates and (d) difference between cellular γ' -precipitates and γ - γ' eutectics observed in the alloy after fatigue test at 750 °C and $\Delta\epsilon/2$ of 0.5 pct (Color figure online).

depicts the difference between cellular γ' -precipitates and γ - γ' eutectics observed in the alloy after fatigue test at 750 °C and $\Delta\epsilon/2$ of 0.5 pct. Alam *et al.*^[34] have observed similar features during the creep deformation studies of the CM 247 LC alloy.

Fracture appearance of the specimen fatigue tested at 750 °C and $\Delta\epsilon/2$ of 0.8 pct (Figures 11(a) and (b)) is similar to the one observed at $\Delta\epsilon/2 = 0.5$ pct, except the presence of a larger cellular γ' -precipitates. It can be seen (Figure 11(c)) that these precipitates along with carbides (Figure 11(d)) act as crack initiation sites.

Figures 12(a) and (b) depicts the fracture surface of the DS alloy fatigue ruptured at $\Delta\epsilon/2$ of 0.5 pct and 850 °C. It can be (Figures 12(a) and (b)) seen that the crack initiation takes place in both transgranular as well as the intergranular manner. Additionally, oxidation appears in grain boundary (Figure 12(c)). Moreover, in contrast to $\Delta\epsilon/2$ of 0.5 pct, only transgranular crack initiation sites are observed in the specimen fatigue tested at $\Delta\epsilon/2$ of 0.8 pct (Figures 13(a) and (b)). Unlike, low amplitude LCF test, here oxidation appears in transgranular cracks. Figure 14(a) through (c) shows the longitudinal section of the specimen fatigue tested at $\Delta\epsilon/2$ of 0.5 pct and 930 °C. A lot of voids can be seen in the microstructure (Figure 14(a)). These voids linked together and forming secondary cracks. Cracks are observed to be formed in the precipitates free zone (PFZ) as shown in Figure 14(b). This PFZ formed as a consequence of the loss of aluminum owing to the oxidation.^[35] As evident, fatigue deformation caused

extensive γ' -coarsening throughout the cross-section (Figure 14(c)).

Figure 14(d) shows the fracture surface of the specimen fatigued at 930 °C and $\Delta\epsilon/2 = 0.5$ pct. Under this scenario, the crack has multiple initiation sites, one such site located at the surface is shown by a rectangle. A lot of dimples were observed on the fracture surface. The dimples are possibly formed due to the linkage of voids seen in Figure 14(a). Figure 15(a) and (b) shows the fractography of the specimen fatigued at 930 °C and $\Delta\epsilon/2 = 0.8$ pct. Like fatigue at 930 °C and $\Delta\epsilon/2 = 0.5$ pct, crack initiation under this condition also takes place from both surface (marked by a circle) and subsurface regions. Fatigue striations (Figure 15(b)) are appearing near the crack initiation site. The presence of these striations indicates that the crack propagates in this direction. Cracks are emanating from the PFZ and make their way inside, the material (Figure 15(c)). The oxidation appears in these cracks (Figure 15(c)). Relatively higher coarsening of γ' (Figure 15(d)) takes place during this condition as compared to the $\Delta\epsilon/2 = 0.5$ pct.

G. Deformation Substructures

A detailed TEM analysis was carried out to assess the effect of temperature on fatigue deformation mechanisms. Substructural evolution during both low ($\Delta\epsilon/2 = 0.5$ pct) and high values ($\Delta\epsilon/2 = 0.8$ pct) of $\Delta\epsilon/2$ were studied. Figures 16(a) and (b) shows the typical deformation substructures of the specimen fatigue tested at

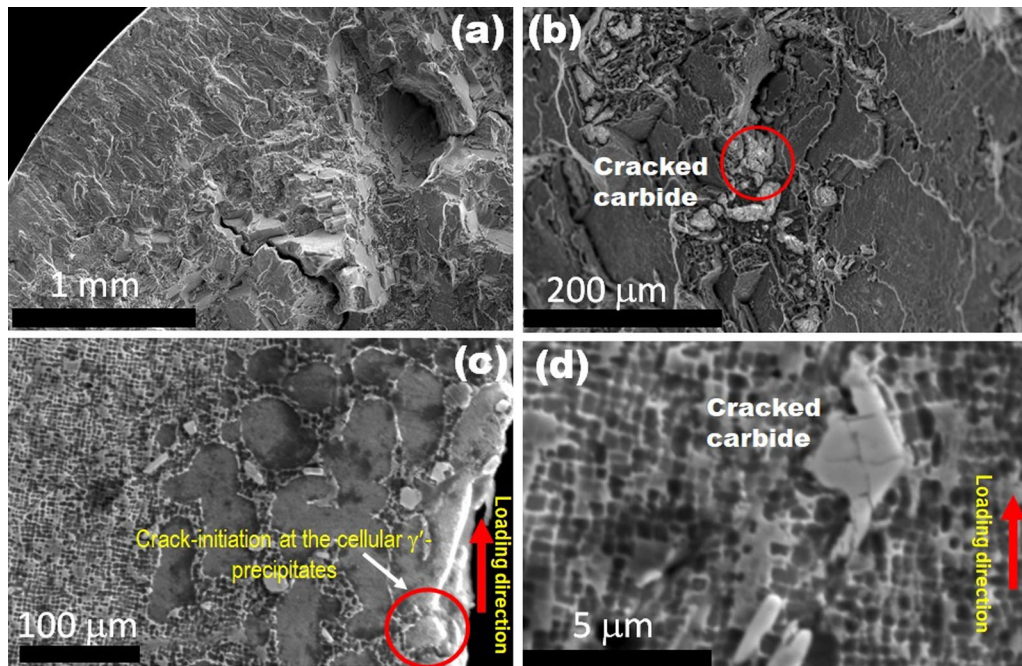


Fig. 11—(a, b) Fracture surfaces and (c, d) SEM micrographs of the specimens fatigued at $\Delta\epsilon/2$ of 0.8 pct and 750 °C. The area marked by yellow circles (b) and a red circle (c) showing the crack initiations at the cellular γ' -precipitates (Color figure online).

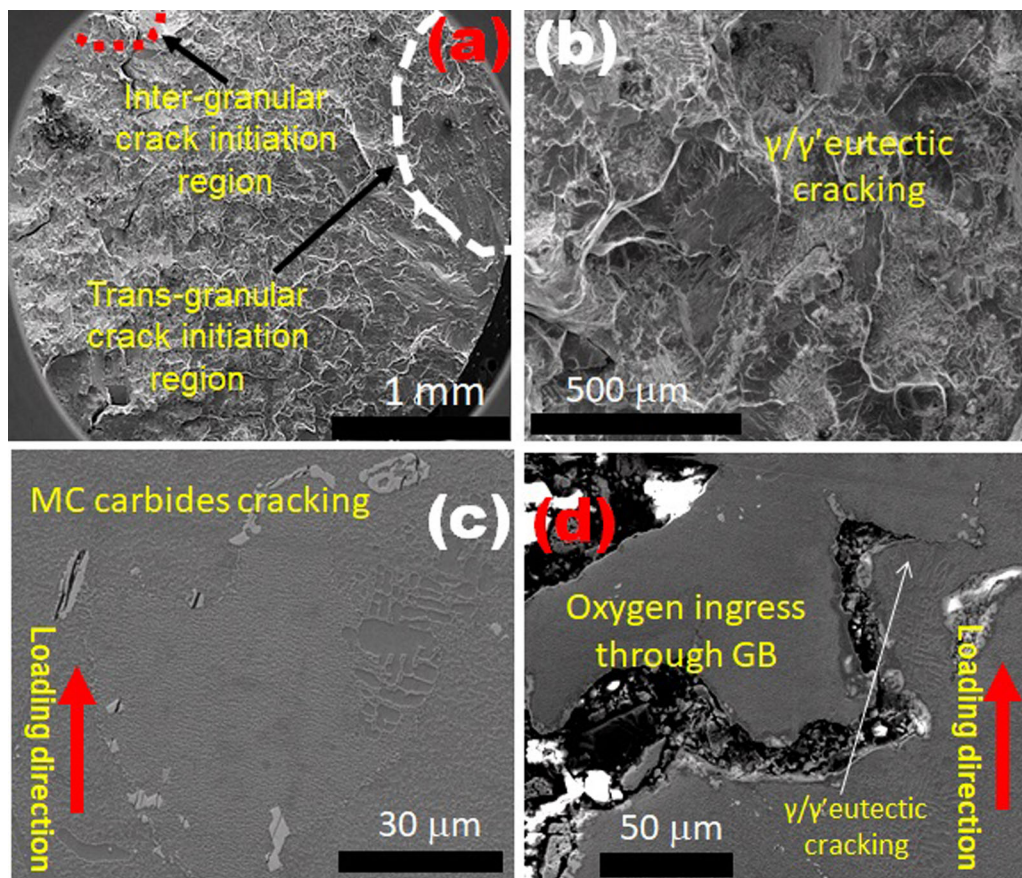


Fig. 12—(a, b) Fracture surfaces and (c, d) SEM micrographs of the specimens fatigued at $\Delta\epsilon/2$ of 0.5 pct and 850 °C.

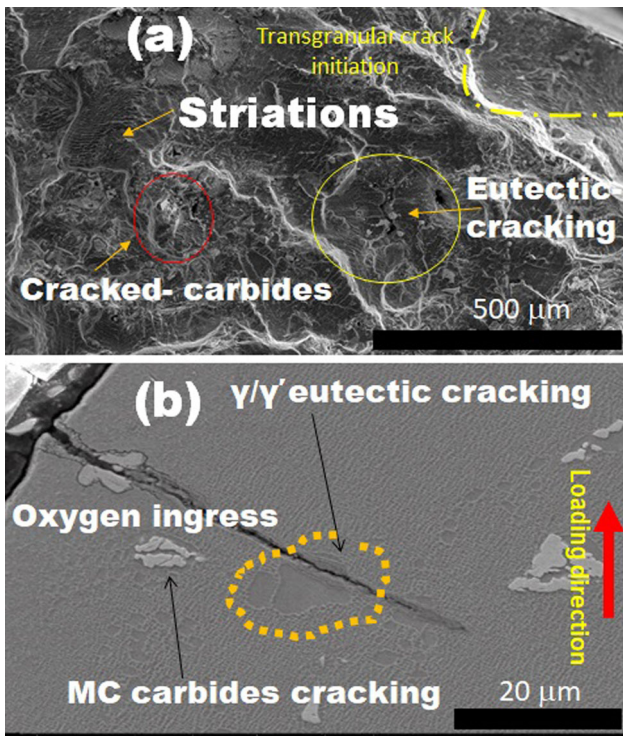


Fig. 13—(a) Fracture surfaces and (b) SEM micrographs of the specimens fatigued at $\Delta\epsilon/2$ of 0.8 pct and 850 °C.

750 °C and $\Delta\epsilon/2 = 0.5$ pct. Stacking faults (SFs) extended to both γ and γ' -precipitates are observed in the TEM micrograph as shown in Figure 16. In addition to that, APB-coupled dislocation pair (shown by arrow) and seldom dislocation network are also observed (Figure 16(b)). The formation of the SFs inside γ' during LCF deformation is widely reported for both DS and SX nickel-based superalloys.^[22,36] However, the presence of SFs inside the γ -matrix is rarely seen, particularly at this temperature. The formation of SFs inside the γ -matrix is due to the lower stacking fault energy (SFE) of the DS alloy.^[17] Dislocation substructures at 750 °C and $\Delta\epsilon/2 = 0.8$ pct (Figures 17(a) and (b)) are similar to the one observed at $\Delta\epsilon/2 = 0.5$ pct.

Prominent dislocation features observed after 850 °C LCF tests are nodes, tangles, dislocation looping around γ' -precipitates, and dislocation network at the γ - γ' interface as shown in Figures 18(a) and (b). Unlike low amplitude fatigue tests, dislocation activities are confined within a few γ' -precipitates in the specimen fatigue tested at 850 °C and $\Delta\epsilon/2$ value of 0.8 pct (Figures 19(a) and (b)). Figure 19 shows that the substructure mainly consists of mixed dislocations and APB-coupled dislocations. Figures 20(a) and (b) depicts the TEM micrographs of the specimen fatigue tested at 930 °C and $\Delta\epsilon/2$ of 0.5 pct. γ' -coarsening and dislocation networks are the dominant features (Figure 20(a)). Additionally, dislocation activities are mostly confined in the γ -matrix channels (Figure 20(b)).

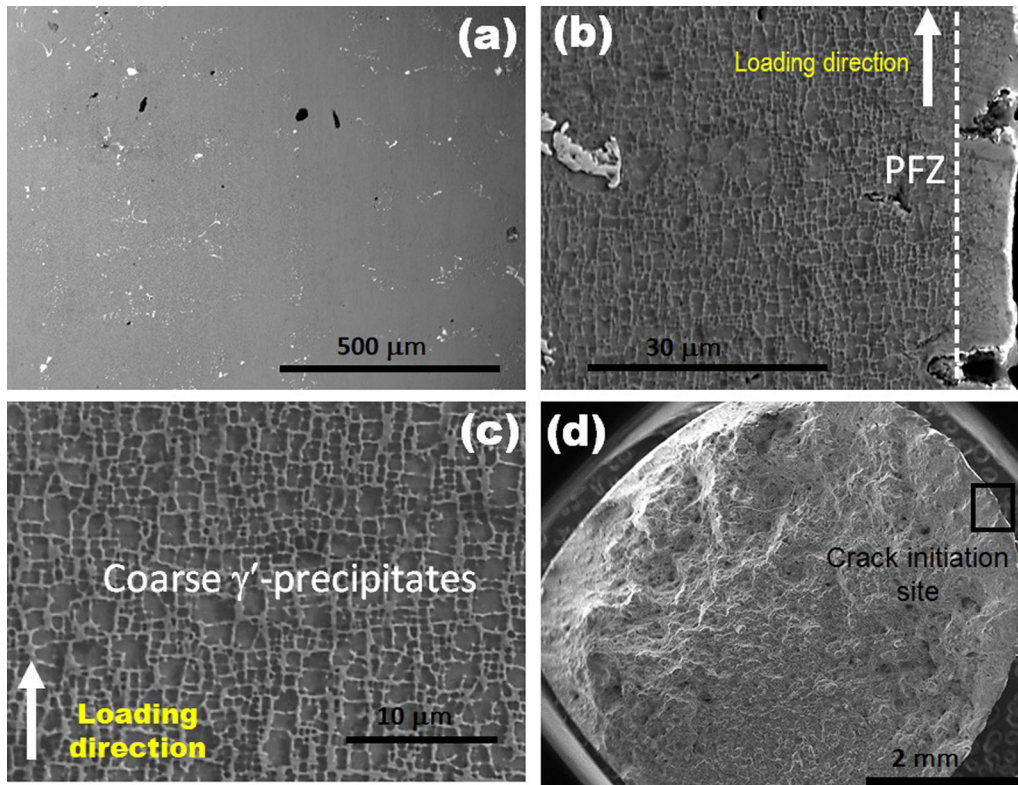


Fig. 14—(a, c) Longitudinal section of the specimen fatigue tested at $\Delta\epsilon/2$ of 0.5 pct and 930 °C. Precipitates free zone (PFZ) is shown in (b). γ' -coarsening is observed in the microstructure (c). (d) The fracture surface of the specimen. The crack initiation site is shown by a rectangle.

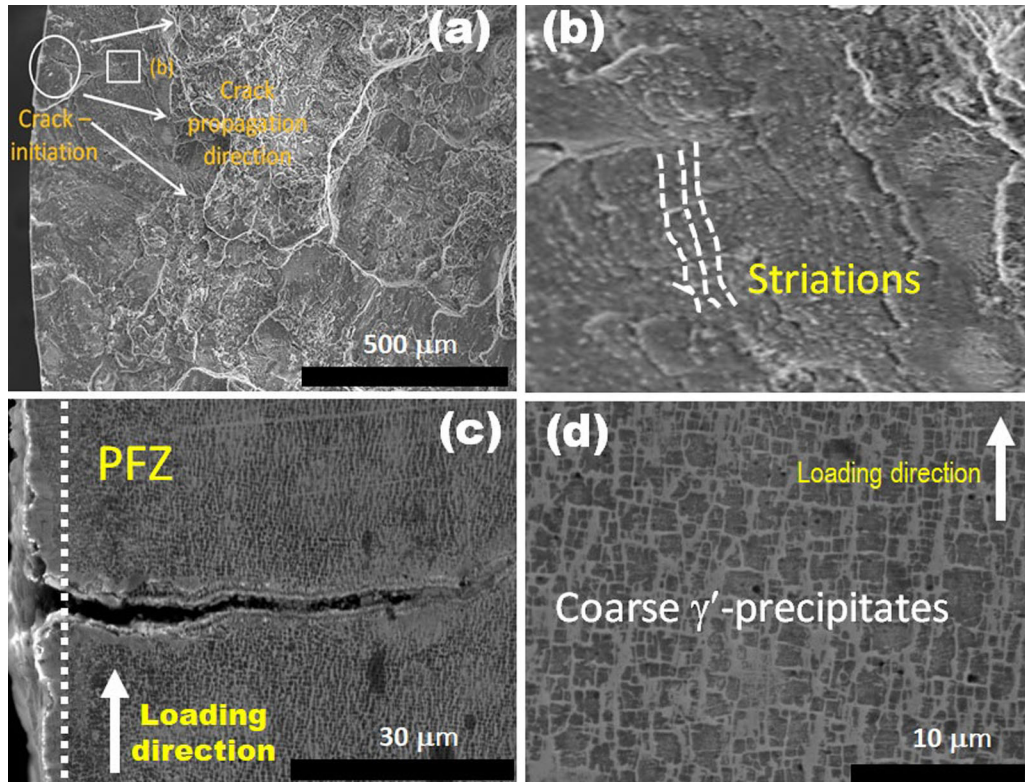


Fig. 15—(a) Fracture surface of the specimen. The crack initiation site is shown by a circle and the crack propagation directions are shown by arrows. (b) a magnified view of the area shown by a rectangle in the image (a). (c, d) Longitudinal section of the specimen fatigue tested at $\Delta\epsilon/2$ of 0.8 pct and 930 °C. Precipitates free zone (PFZ) is shown in (c). γ' -coarsening is shown in (d).

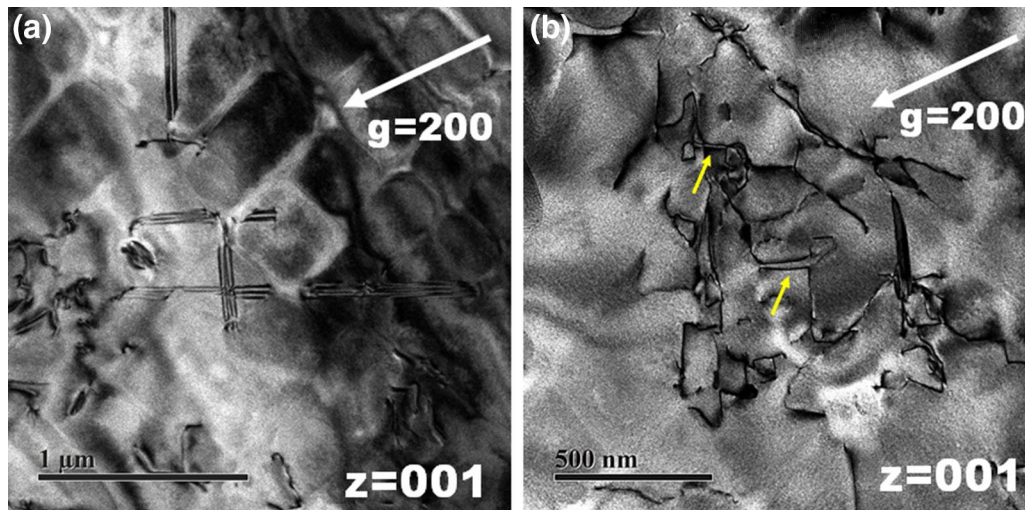


Fig. 16—(a, b) TEM micrographs of specimens fatigued at 750 °C and $\Delta\epsilon/2$ of 0.5 pct, APB-coupled dislocations are shown by the arrow.

IV. DISCUSSION

It is apparent that the cyclic stress response (Figure 5) of the DS alloy is highly sensitive to the testing temperature. At 850 °C and 930 °C (Figures 5(b) and (c)), the alloy exhibited continuous softening behavior, which is in sharp contrast to the initial hardening observed at 750 °C (Figure 5(c)). This fact is well supported by the SWT plots (Figure 9), which are showing different slopes at different temperatures. The

distinct deformation feature observed at these temperatures is possibly responsible for the divergence in associated cyclic stress responses. To ascertain this fact, TEM investigation was conducted on the fatigue-fractured specimens under pertaining conditions. The dislocation substructures of the specimen fatigue fractured at 750 °C, 850 °C, and 930 °C are illustrated in Figures 16, 17, 18, 19 and 20. SFs spanning over the γ/γ' interfaces and sparsely dispersed dislocation networks are found to

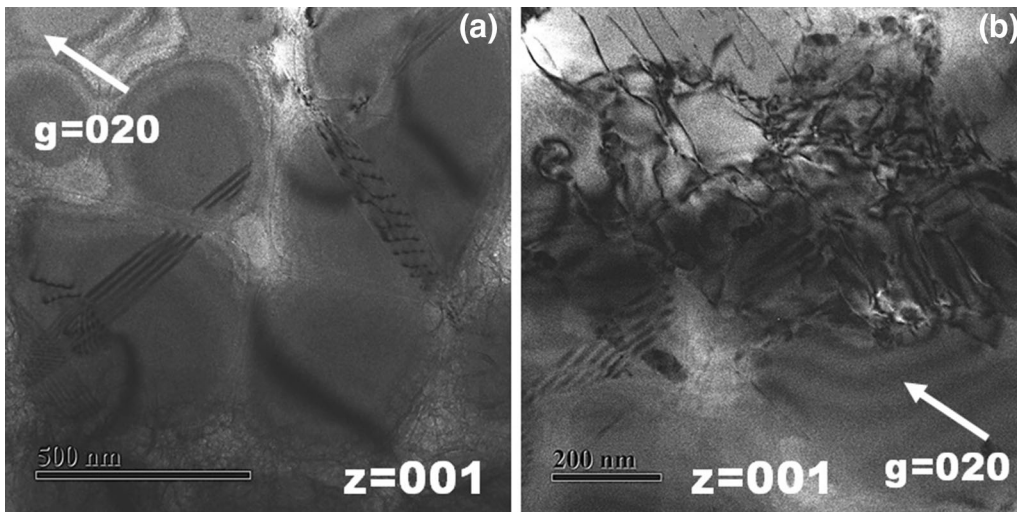


Fig. 17—(a, b) TEM micrographs of specimen fatigued at 750 °C and $\Delta\epsilon/2$ of 0.8 pct.

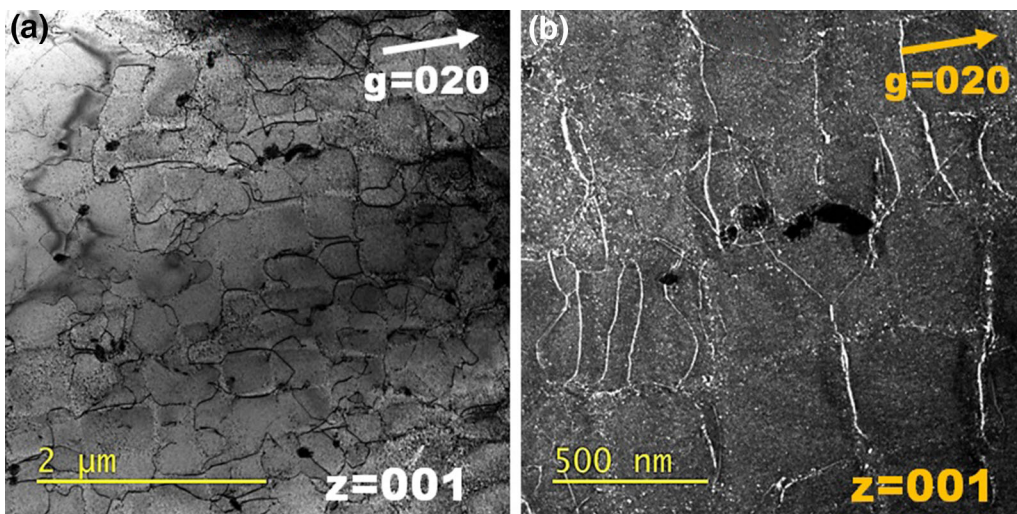


Fig. 18—(a, b) TEM micrographs of specimen fatigued at 850 °C and $\Delta\epsilon/2$ of 0.5 pct.

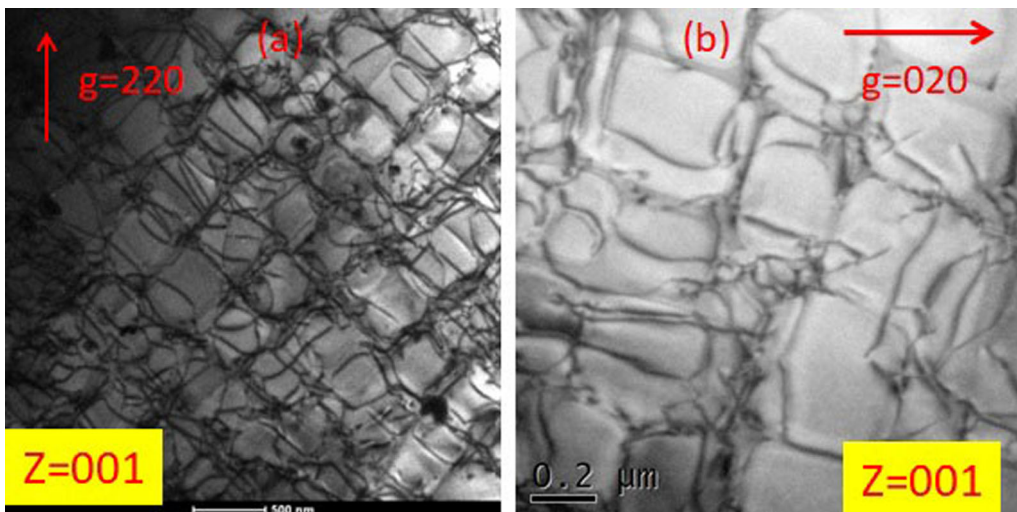


Fig. 19—(a, b) TEM micrographs of specimen fatigued at 850 °C and $\Delta\epsilon/2$ of 0.8 pct.

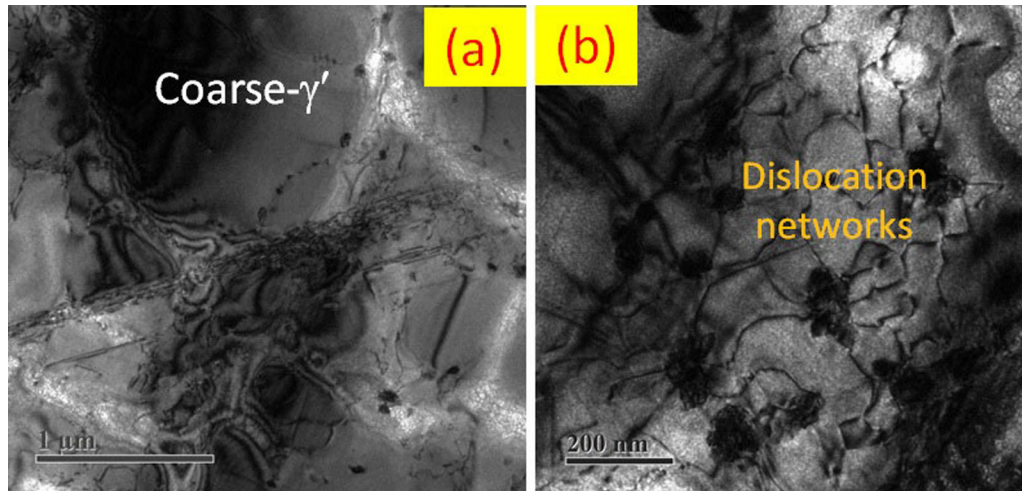


Fig. 20—TEM micrographs of the specimen fatigued at 930 °C and $\Delta\epsilon/2$ of 0.5 pct showing; (a) γ' -coarsening, (b) dislocation networks.

be the prominent deformation features at 750 °C for the $\Delta\epsilon/2$ values of 0.5 and 0.8 pct (Figures 16(a), (b) and 17(a), (b)). However, for the same strain amplitudes, dislocation pile-up at γ/γ' interface, dislocation networks, and loops are dominant at 850 °C and 930 °C (Figures 18, 19 and 20). It is believed that the existence of SFs spanning over the γ/γ' interfaces (Figures 16(a) and 17(a)) are accounted for the initial hardening observed at 750 °C. It is, therefore, very important to understand the underlying mechanism of the formation of such configuration. Li *et al.*^[37] have reported that such configurations are formed by the uncorrelated movement of $a/6 \langle 211 \rangle$ and $a/3 \langle 211 \rangle$ dislocation partials through the alloy. Wang *et al.*^[22] has observed similar deformation features during the low cycle fatigue deformation of a single crystal nickel-based superalloy and accounted for them for the observed cyclic hardening behavior of the alloy. They^[22] have reported that it is very difficult for $a/3 \langle 112 \rangle$ dislocation partial to cut through the γ/γ' interface unless the applied stress is high enough. In the present case, it is evident (Figure 6) that the alloy experiences the highest saturated stress at 750 °C. Additionally, the width of the γ -channel is very narrow. Therefore, it is very likely for $a/3 \langle 112 \rangle$ partial dislocations to shear across the γ/γ' interface and causing the observed hardening. The decrease in the peak stress ($\Delta\sigma/2$) value after initial hardening (Figure 5(a)) at the temperature of 750 °C suggests that some softening mechanism starts dominating over the hardening mechanism operative until then. Deformation curves (Figures 5(b) through (c)) at 850 °C and 930 °C illustrate that the alloy exhibits continuous softening for all the investigated values of $\Delta\epsilon/2$. Therefore, a detailed investigation was carried out to understand the mechanisms for cyclic softening. It is noteworthy that the cyclic softening behavior in the precipitation-hardened nickel-based superalloys is mainly attributed to (i) shearing of the γ' -precipitates, (ii) the presence of dislocation network at the γ/γ' interface, and (iii) coarsening of the precipitates.^[10,11,17,28] Shearing of γ' -precipitates by APB-coupled dislocation partials and

sparsely formed dislocation networks (Figures 16(b) and 17(b)) are mainly responsible for the cyclic softening at 750 °C, whereas, at 850 °C and 930 °C, intense dislocation networking at the γ/γ' interfaces can explain the softening effect. Precipitate coarsening (Figures 14(d) and 15(d)) leads to the additional softening at 930 °C.

It is evident (Figure 4) that the fatigue lives of the alloy are highest at 750; however, those at 850 °C and 930 °C are much shorter especially at the lower values of $\Delta\epsilon/2$. To understand the discrepancies in fatigue life, SEM and TEM analyses of the fatigue ruptured specimens were carried out and discussed in the ensuing paragraphs. It is believed that during the early stage of fatigue deformation at 750 °C, each $a/3 \langle 112 \rangle$ partials glide on only one of the several $\{111\}$ types of octahedral slip plane. Therefore, extended slip planarity is observed before the duplex/multiple slips activated. The presence of the continuous SFs extending to both matrix and precipitates (Figures 16(a) and 17(a)) supports these facts. An increased cyclic life observed at this temperature is possibly due to the accumulation of large strain, resulting from slip planarity.

The highest fatigue life observed at 750 °C can be also comprehended if it is assessed as a function of plastic strain amplitude ($\Delta\epsilon_p/2$). As $\Delta\epsilon_p/2 = \Delta\epsilon/2 - (\Delta\sigma/2E)$, the value of $\Delta\epsilon_p/2$ at any $\Delta\epsilon/2$ depends on the flow stress and E . It is evident from Figure 6 that flow stress is highest at 750 °C. Additionally, there are not many changes in E value in the given temperature range. The ratio of $\Delta\sigma/2E$ at 750 °C, 850 °C, and 930 °C for the investigated range of $\Delta\epsilon/2$ is given in Table II. For the investigated superalloy, as T increases from 750 °C to 930 °C, the ratio of $\Delta\sigma/2E$ decreases (Table II), and therefore, $\Delta\epsilon_p/2$ at 750 °C is lower than that at 850 °C and 930 °C and is considered to be one of the main reasons for the higher fatigue lives at 750 °C.

However, at 850 °C and 930 °C, reduction in fatigue life is attributed to the formation of intense dislocation networks. The formation of such heterogeneous dislocation networks leads to the strain localization and

premature failure of the material. Figure 18(b) shows one such area where cracks are initiated near dislocation networks.

Since there is no significant difference in the substructures observed at temperatures of 850 °C and 930 °C, therefore, cyclic life at these temperatures is expected to be similar. However, a significant decrease in fatigue lives is observed at 930 °C.

This implies that additional detrimental factors are operating at this temperature. Since the discrepancies in fatigue lives are more prominent at the lower values of $\Delta\epsilon/2$. Therefore, it is pertinent to assume that the reduction in fatigue life is arising out of oxidation. In addition to that, the detrimental effect of sustained mean stress developed at the lower values of $\Delta\epsilon/2$ is an additional contributing factor for the lower fatigue life.

Figures 10, 11, 12, 13, 14, and 15 illustrate the fractured surfaces and longitudinal sections of the ruptured LCF-tested specimens. It is evident that (Figures 10, 11, 12, 13, 14, and 15) the surface-initiated fatigue failure modes have prevailed at all the investigated temperatures. At 750 °C, the cracks are mostly initiated from the cellular γ' -precipitates formed at the specimen surface (Figures 10(c) and 11(c)). At 850 °C, cracks are found to be initiated from the surface oxide layer during fatigue cycling and make its way into the bulk specimen, either transgranular (Figure 13(b)) or intergranular (Figure 12(d)). However, at 930 °C, the cracks are observed to be formed in the PFZs (Figures 14(b) and 15(c)). It has been seen that^[28,29] the PFZs are formed as a consequence of oxidation and are one of the main culprits for the reduction of fatigue life at 930 °C. The PFZ formed at the surface is relatively much weaker than the rest of the matrix. Therefore, its existence deteriorates the overall LCF properties. The deleterious effect of such a factor has been observed during the creep deformation of many nickel-based superalloys.^[28,29] From the above discussion, it can be suggested that the resistance to the oxidation is very crucial for the DS alloy, especially when it is exposed above 850 °C.

In addition to that, it is worth to notice that, the microconstituents also playing a crucial role during the deformation. At $T = 750$ °C, the formation of cellular γ' -precipitates provides a site for crack nucleation (Figure 10(c)) whereas at $T = 850$ °C and 930 °C, the degeneration of γ' -precipitates (coarsening) (Figures 14(c) and 15(d)), the formation of PFZs (Figures 14(b) and 15(c)), and carbides (Figures 12(c) and 13(b)) dictate the fatigue deformation behavior of

the alloy. A more detailed study is required to understand the role of constituent phases on the cyclic deformation behavior of the alloy and out of the purview of this study.

The present study reveals that the decrease in fatigue life of the DS alloy with an increase in temperature is attributed to the synergistic effect of substructures generated during deformation, instability of the constituent phases, and oxidation.

V. CONCLUSIONS

Following conclusions are drawn from the present study:

- I. The decrease in fatigue life of the investigated superalloy with increasing temperature is ascribed to the combined effect of substructural evolution and instability of the constituent phases allowing increasing plastic strains, as well as oxidation effects.
- II. Fatigue deformation mechanism of the investigated superalloy changes as a function of temperature. At the lowest temperature, *i.e.*, at 750 °C, shearing of γ' -precipitates by SSFs is the dominant deformation mechanism, whereas at the highest temperature, *i.e.*, at 930 °C, γ' -coarsening and the formation of dislocation networks are dominant. At 850 °C, a mixed deformation mechanism is observed.
- III. Microconstituents have significant impacts on the fatigue deformation mechanism of the investigated superalloy. Cellular γ' -precipitates provide a site for crack nucleation at 750 °C, whereas at 850 °C and 930 °C, the degeneration of γ' -precipitates (coarsening/PFZ) dictates the fatigue deformation mechanism.

REFERENCES

1. K. Harris, G.L. Erickson, and R.E. Schwer: *Superalloys*, 1984, vol. 1984, pp. 221–30.
2. M.V. Nathal, R.A. Mackay, and R.G. Garlick: *Mater. Sci. Eng.*, 1985, vol. 75, pp. 195–205.
3. I.S. Kim, B.G. Choi, H.U. Hong, Y.S. Yoo, and C.Y. Jo: *Mater. Sci. Eng. A*, 2011, vol. 528 (24), pp. 7149–55.
4. J. Grodzki, N. Hartmann, R. Rettig, E. Affeldt, and R.F. Singer: *Metall. Mater. Trans. A*, 2016, vol. 47A, pp. 2914–26.
5. J.T. Guo, C. Yuan, H.C. Yang, V. Lupinc, and M. Maldini: *Metall. Mater. Trans. A*, 2001, vol. 32A, pp. 1103–10.
6. M. Valsan, D.H. Sastry, K.B. Sankara Rao, and S.L. Mannan: *Metallurgical and Materials Transactions A*, 1994, vol. 25, pp. 159–71.
7. J. Tong, S. Dalby, J. Byrne, M.B. Henderson, and M.C. Hardy: *Int. J. Fatigue*, 2001, vol. 23, pp. 897–902.
8. M. Maldini, M. Marchionni, M. Nazmy, M. Staubli, and G. Osinkolu: *Creep and fatigue properties of a directionally solidified nickel base superalloy at elevated temperature*, The Metallurgical Society, Warrendale, PA, 1996, pp. 327–34.
9. R.J. Kashinga, L.G. Zhao, V.V. Silberschmidt, F. Farukh, N.C. Barnard, M.T. Whittaker, D. Proprentner, B. Shollock, and G. McColvin: *Mater. Sci. Eng. A*, 2017, vol. 708, pp. 503–13.

Table II. Values of $\Delta\sigma/2E$ at the Investigated Temperatures

$\Delta\sigma/2E$			
$T = 750$ °C	$T = 850$ °C	$T = 930$ °C	$\Delta\epsilon/2$ [Pct]
0.80	0.54	0.46	0.4
0.79	0.66	0.59	0.6
0.87	0.70	0.68	0.7
0.94	0.77	0.74	0.8

10. H. Zhou, Y. Ro, H. Harada, Y. Aoki, and M. Arai: *Mater. Sci. Eng. A*, 2004, vol. 381, pp. 20–27.
11. P. Li, Q.Q. Li, T. Jin, Y.Z. Zhou, J.G. Li, X.F. Sun, and Z.F. Zhang: *Int. J. Fatigue*, 2014, vol. 63, pp. 137–44.
12. A Nagesha, M Valsan, R Kannan, K Bhanu Sankara Rao, and SL Mannan: *Int. J. Fatigue*, 2002, vol. 24, pp. 1285–93.
13. M. Marchionni, G.A. Osinkolu, and M. Maldini: *Fatigue Fract. Eng. Mater. Struct.*, 1996, vol. 19, pp. 955–62.
14. A. Pineau and S.D. Antolovich: *Eng. Fail. Anal.*, 2009, vol. 16, pp. 2668–97.
15. R. Rahouadj, J. Menigault, and M. Clavel: *Mater. Sci. Eng.*, 1987, vol. 93, pp. 181–90.
16. H. Tsuji and T. Kondo: *J. Nucl. Mater.*, 1987, vol. 150, pp. 259–65.
17. R.K. Rai, J.K. Sahu, S.K. Das, N. Paulose, D.C. Fernando, and C. Srivastava: *Mater. Charact.*, 2018, vol. 141, pp. 120–28.
18. M Valsan, P Parameswaran, K Bhanu Sankara Rao, M Vijayalakshmi, SL Mannan, and DH Shastry: *Metall. Mater. Trans. A*, 1992, vol. 23A, pp. 1751–61.
19. T.P. Gabb, J. Gayda, and R.V. Miner: *Metall. Mater. Trans. A*, 1986, vol. 17A (3), pp. 497–505.
20. Z.F. Yue and Z.Z. Lu: *Metall. Mater. Trans. A*, 1995, vol. 26A (7), pp. 1815–21.
21. J.H. Zhang, Z.Q. Hu, Y.B. Xu, and Z.G. Wang: *Metall. Mater. Trans. A*, 1992, vol. 23A, pp. 1253–58.
22. X.G. Wang, J.L. Liu, T. Jin, X.F. Sun, Y.Z. Zhou, Z.Q. Hu, J.H. Do, B.G. Choi, I.S. Kim, and C.Y. Jo: *Scripta Mater.*, 2015, vol. 99, pp. 57–60.
23. M Gell and GR Leverant: *Fatigue at Elevated Temperatures*, ASTM International, Philadelphia, 1973, pp. 37–67.
24. H. Mughrabi: *Mater. Sci. Technol.*, 2009, vol. 25, pp. 191–204.
25. R.K. Rai, J.K. Sahu, A. Pramanick, N. Paulose, D.C. Fernando, and S.K. Das: *Mater. Charact.*, 2019, vol. 150, pp. 155–65.
26. R.K. Rai, J.K. Sahu, P.S.M. Jena, S.K. Das, N. Paulose, and D.C. Fernando: *J. Mater. Eng. Perform.*, 2018, vol. 27 (2), pp. 659–65.
27. R.K. Rai, J.K. Sahu, P.S.M. Jena, S.K. Das, N. Paulose, and C.D. Fernando: *Mater. Sci. Eng. A*, 2017, vol. 705, pp. 189–95.
28. Z. He, Y. Zhang, W. Qiu, H.-J. Shi, and J. Gu: *Mater. Sci. Eng. A*, 2016, vol. 676, pp. 246–52.
29. R.K. Rai and J.K. Sahu: *Mater. Lett.*, 2018, vol. 230, pp. 241–44.
30. A. Ince and G. Glinka: *Fatigue Fract. Eng. Mater. Struct.*, 2011, vol. 34, pp. 854–67.
31. N.E. Dowling: *Mean Stress Effects in Stress-Life and Strain-Life Fatigue*, 2004.
32. M Valsan, DH Sastry, KB SankaraRao, and SL Mannan: *Metall. Mater. Trans. A*, 1994, vol. 25A, pp. 159–71.
33. R.K. Rai and J.K. Sahu: *Mater. Sci. Technol.*, 2019, vol. 35, pp. 1220–26.
34. M.Z. Alam, D.V. Satyanarayana, D. Chatterjee, R. Sarkar, and D.K. Das: *Procedia Eng.*, 2013, vol. 55, pp. 835–41.
35. R. Maldonado and E. Nembach: *Acta Mater.*, 1997, vol. 45, pp. 213–24.
36. J.X. Zhang, H. Harada, Y. Ro, Y. Koizumi, and T. Kobayashi: *Acta Mater.*, 2008, vol. 56, pp. 2975–87.
37. Y. Li, F. Pyczak, J. Paul, M. Oehring, U. Lorenz, Z. Yao, and Y. Ning: *Mater. Sci. Eng. A*, 2018, vol. 719, pp. 43–48.

Publisher's Note Springer Nature remains neutral with regard to jurisdictional claims in published maps and institutional affiliations.